POLITECNICO DI TORINO
Repository ISTITUZIONALE

Design Principles and Insights into the Liquid-Phase Exfoliation of Alpha-MoO3 for the Production of Colloidal 2D Nano-inks in Green Solvents

Original
Design Principles and Insights into the Liquid-Phase Exfoliation of Alpha-MoO3 for the Production of Colloidal 2D Nano-inks in Green Solvents / Crisci, M., Dolcet, P., Yang, J., Salerno, M., Belteky, P., Kukovecz, A., Lamberti, F., Agnoli, S., Osella, S., Gross, S., Gatti, T.. - In: JOURNAL OF PHYSICAL CHEMISTRY. C. - ISSN 1932-7447. - 126:1(2022), pp. 404-415. [10.1021/acs.jpcc.1c09221]

Availability:
This version is available at: 11583/2975580 since: 2023-02-13T11:49:07Z

Publisher:
ACS

Published
DOI:10.1021/acs.jpcc.1c09221

Terms of use:

This article is made available under terms and conditions as specified in the corresponding bibliographic description in the repository

Publisher copyright
ACS postprint/Author's Accepted Manuscript

This document is the Accepted Manuscript version of a Published Work that appeared in final form in JOURNAL OF PHYSICAL CHEMISTRY. C, copyright © American Chemical Society after peer review and technical editing by the publisher. To access the final edited and published work see http://dx.doi.org/10.1021/acs.jpcc.1c09221.

(Article begins on next page)

09 November 2026

Design principles and insights into the liquid-phase exfoliation of alpha-MoO_3 for the production of colloidal 2D nano-inks in green solvents

Matteo Crisci,[1] Paolo Dolcet,[2] Jijin Yang,[3] Marco Salerno,[4] Péter Bélteky,[5] Ákos Kukovecz,[5] Francesco Lamberti,[3] Stefano Agnoli,[3] Silvio Osella,[6*] Silvia Gross,[2,3*] Teresa Gatti[1*]

[1] Center for Materials Research, Justus Liebig University, Heinrich-Buff-Ring 17, 35392 Giessen, Germany

[2] Institute for Chemical Technology and Polymer Chemistry, Karlsruhe Institute of Technology (KIT), D-76131, Karlsruhe, Germany

[3] Department of Chemical Sciences, University of Padua, via Marzolo 1, 35131 Padova, Italy

[4] Materials Characterization Facility, Italian Institute of Technology, Via Morego 30, 16163 Genova, Italy

[5] Interdisciplinary Excellence Centre, Department of Applied and Environmental Chemistry, University of Szeged, Rerrich Béla tér 1, H-6720 Szeged, Hungary

[6] Chemical and Biological Systems Simulation Lab, Center of New Technologies, University of Warsaw, Banacha 2C, 02-097 Warsaw, Poland

E-mail: s.osella@cent.uw.edu.pl ; silvia.gross@unipd.it ; teresa.gatti@phys.chemie.uni-giessen.de

Abstract

The interest in layered 2D nanomaterials has witnessed an impressive growth in the last few years, bringing to the discovery of many new species and different methods for their preparation. The liquid-phase exfoliation (LPE) of crystalline bulk powders is certainly the most suitable method for a scaled-up production, allowing also the convenient access to solution processing techniques for the direct utilization of the produced 2D material colloidal inks. Given the large number of reports on LPE processes for different 2D materials, today it is necessary to define in detail the results of similar investigations, so as to provide the scientific community with specific guidelines for identifying design rules and applying standardized procedures. In this work, we present a systematic study on the LPE process for α-MoO_3, a very stable high band gap semiconductor, which in its 2D form has been employed for many purposes, ranging from catalysis to energy/optoelectronic devices and sensing. We investigate the effect of different low-toxicity solvents and instruments for the LPE of this material and provide new insights into the structural and electronic properties of the resulting 2D nano-inks in a joint experimental-computational effort, which will represent a solid source of information for the future implementation of liquid-dispersed layered α-MoO_3 nanosheets in different fields.

Keywords

α-MoO_3, 2D material colloidal ink, 2D MoO_3, liquid-phase exfoliation, green solvent

1. Introduction

In the past years, many research efforts have been directed towards the identification of species that can be used in substitution of the so-called critical raw materials for different vital applications, with the aim of preventing a global supply crisis driven by the progressive increasing demand of technological items.[1] In this context, metal oxide semiconductors emerge as a valuable platform to obtain new substitute materials, considering their chemical stability and ease of tunability in functional properties, achievable through different methods, ranging from doping to dimensional variation from the bulk to the diversified nanoforms.[1]

Molybdenum trioxide (MoO_3) emerges as a suitable candidate for this role: Mo is indeed a non-critical raw material and its oxide is an interesting semiconductor, characterized by a high band gap, high work function and notable environmental stability.[2–7] This material attracts interest for a very wide range of applications: there are numerous reports on its use for electro-, thermo- and photochromism,[8–11] catalysis,[12,13] Li ion batteries[14,15] and solar cells,[16,17] demonstrating its versatility in different functions.

MoO_3 can display three main crystalline phases, namely the highly stable α- and h-phases and the metastable β-phase. In these phases, MoO_6 octahedra are always present as basic structural units but they differ in their relative connectivity. In the α-one, the MoO_6 octahedra organize in order to form an orthorhombic cell that results from the overlap of different MoO_3 layers, where they are connected by sharing oxygen corners, while these layers are held together by van der Waals forces. The β-phase is a metastable monoclinic phase that resemble the structure of ReO_3, while the h-phase has a hexagonal structure where octahedra are connected *via* corner sharing oxygen atoms that form long linear chains.[18,19] The α-phase is the most investigated one, due to its layered structured, which makes α-MoO_3 similar to other layered materials, such as the transition metal dichalcogenides (TMDs) MoS_2, WS_2, and the corresponding selenides and tellurides,[20] making it suitable for exfoliation processes leading to the formation of the corresponding material in bidimensional (2D) form. 2D MoO_3 is an emerging 2D material, together with other 2D metal oxides, investigated for similar purposes as the 3D counterpart, but offering more promising perspectives in terms of high surface to volume ratio, which favors interfacial exchanges with charges or molecules, adsorbates and other nanomaterials.[21–24]

The liquid-phase exfoliation (LPE) is a particularly convenient top-down process for the production of 2D materials as colloidal inks, suitable for subsequent direct utilization or processing, which can be carried out through shear mixing (SM) or tip sonication (TS) in a liquid-dispersed phase.[25–29] Several liquid media can be employed for this purpose, the most

effective generally being organic high boiling point solvents, such N-methylpyrrolidone (NMP),[30,31] or dimethylformamide (DMF),[32,33] and dimethyl sulfoxide (DMSO),[34,35] which have all led to 2D material inks with very high concentration, but that hold considerable drawbacks related to the difficulties in removing them during processing and to the toxicity and high cost issues.[36,37] For this reason, research aiming at resorting to non-toxic solvents during LPE,[38] such as water[39–42] or alcohols [43,44] is progressively attracting increasing interest from the scientific community. However, these green solvents, when used as the sole dispersants, have some limitations connected to the relatively low concentration in final 2D materials that they allow to reach, being often necessary to resort to the assistance of surfactants to improve their stability, [36] which can then compromise the electronic properties of solution-processed thin films through their insulating effect.

In this work, we present a systematic investigation on the LPE of α-MoO_3 crystalline powder in a series of green solvents characterized by relatively low boiling points without the help of any dispersant, allowing to define the best media to produce good quality 2D α-MoO_3 nano-inks. We also compare the effect of resorting to SM or TS exfoliating instruments and of protracting the process for different times and look in detail at the physico-chemical and morphological properties of the resulting colloids. Advanced structural analysis achieved by resorting to X-ray absorption spectroscopy (XAS) provides new insights into the structure of α-MoO_3 2D nanosheets which have been never reported before, to the best of our knowledge. These data, combined with density functional theory (DFT) investigations, allow to shed new light onto the properties of this emerging 2D semiconductor[45] which might serve as guidelines for its future implementation in energy-related or optoelectronic devices as well as for its use in sensing and catalysis.

2. Materials and methods

All chemicals were purchased from Sigma Aldrich and used without any further purification. α-MoO_3 was synthesized using an already reported procedure developed by some of us.[46] Technical grade isopropanol was used for LPE. UV-Visible (UV-vis) absorption spectra of the colloidal inks were measured on a Goebel Uvikon spectrometer using a quartz cuvette of 1 cm optical length. Raman spectra were measured on a Bruker Senterra instrument, using a 514 nm laser excitation source. Samples were prepared by drop casting the suspensions over a silicon slide and then analyzed. Zeta Potential (ZP) was measured on a Malvern Zetasizer Nano-ZS device. The samples were measured in Rotilabo precision glass cuvettes with a light path of 10 mm and a volume of 3.5 mL. High resolution transmission electron microscopy (HR-TEM) images and selective area electron diffraction (SAED) patterns were acquired on a FEI Tecnai G2 20 X Twin TEM operating at 200 kV. Powder X-ray diffraction (P-XRD) analysis was

performed at ambient temperature with a PANalytical B.V. X'Pert PRO diffractometer employing Cu Kα1 radiation. The instrument operated at 40 kV and 40 mA using a 1° divergence slit for the incident beam. Atomic force microscopy and Kelvin-probe force microscopy (AFM and KPFM) were both carried out on a MFP-3D atomic force microscope by Asylum Research-Oxford Instruments, using NCHV probes, of highly-doped (0.01-0.025 Ω cm) n-type (An-doped) Silicon, with nominal cantilever resonance frequency of 320 kHz and tip apex radius of curvature of 8 nm, operated in Nap (i.e. double-pass) mode at a typical elevation height of 50 nm. X-ray photoelectron spectroscopy (XPS) measurements were performed in a custom-designed ultra-high vacuum chamber, working at base pressure of 10^{-9} mbar, equipped with a non-monochromatized dual-anode DAR 400 X-ray source, a 5-channeltrons and an Omicron EA 125 electron analyzer. The XPS data were collected at room temperature with an Al Kα line (1486.7 eV) using 0.1 energy steps, 0.5 s dwell time and 20 eV pass energy. The calibration was based on the binding energy (B.E.) of the Au4f7/2 line at 83.9 eV with respect to the Fermi level. The standard deviation for the B.E. values was 0.15 eV. The reported B.E. were corrected for the B.E. charging effects, assigning the B.E. value of 284.6 eV to the C1s line of carbon. XAS spectra were collected at the SAMBA beamline of the SOLEIL synchrotron facility (Gif-sur-Yvette, France). Data were collected at Mo K-edge, using a Si(220) crystal monochromator for energy selection (energy resolution ca. $6 \cdot 10^{-15}$). Powdered samples were pressed into pellets, using cellulose as binder, and measured in transmission mode, using Oxford ionization chambers as detectors. Samples in liquid suspension were recorded in fluorescence mode, exploiting a 35-elements Ge detector.

2.1 LPE of α-MoO_3 powder

To produce the bulk α-MoO_3 suspension in a liquid environment, 1 g of the powder material was dispersed in 100 mL of the chosen solvent (water, isopropanol/water 6:4 v/v, acetone, 2-butanone). Then, the resulting slurry was pre-sonicated for 30 minutes in a bath-sonicator (Elma, Elmaosonic P) in order to disperse completely the material. This was then followed by LPE *via* SM (on an IKA T 25 digital Ultra-Turrax instrument), operating at 8000 rpm or *via* tip TS (on a Bandelin Sonopuls HD2200 instrument) operated at 80 % power using pulses of 3 s on/3 s off. Both operations were carried out for three different times (2, 4 and 8 hours). Once the LPE process was completed, liquid cascade centrifugation was applied to separate the different species in suspensions based on relative size and thickness, so as to isolate a final colloid containing the most exfoliated fractions. The resulting suspension were thus centrifuged first at 1500 rpm (210 rcf) for 1 hour and then the supernatant was carefully removed and centrifuged again at 3000 rpm (837 rcf) for 1 hour. This final supernatant was recovered as the target colloidal ink and used for characterizations. The concentration of these final inks was calculated

by either drying 10 mL of the suspension in a previously weighted Petri dish and calculating the difference in weight or by filtering 5 mL of the suspension through a previously weighted PTFE filter and calculating the difference in weight after drying the filter in a vacuum oven at 40 °C overnight.

2.2 Computational analysis of bulk and 2D α-MoO_3

The α-MoO_3 3D orthorhombic crystal structure was considered as input structure for *ab initio* calculations carried out at the DFT periodic protocol within the PWscf package of the Quantum Espresso 5.1 program.[47] Geometry optimization was performed with scalar relativistic pseudopotentials,[48] with the PBEsol functional,[49] together with a wavefunction and density cutoff of 50 and 400 Ry, respectively. A 18 x 6 x 18 k-sampling was considered for the analysis of the first Brillouin zone, and band structures, density of states (DOS) and work function shift analyzed. From the optimized 3D α-MoO_3 structure, a 2D slab has been extracted and the geometry optimized at the same level of theory, with now a 18 x 1 x 18 k-sampling (the y-axis has been considered as the direction normal to the plane of the slab).

For the *ab initio* X-ray Absorption Near Edge Structure (XANES) calculations, the parallel version of the FDMNES package was used.[50,51] The FDMNES code features real-space monoelectronic calculations. The final state was calculated using the finite different method (FDM) of the FDMNES code; this method is a full potential one and introduces no approximation on the shape of the potential. The XANES contributions of the Mo sites were calculated using a cluster radius of 7 Å. A convolution procedure was applied to the calculated spectra to account for the core-hole lifetime and multi-electron excitations.

3. Results and discussion

In previous works, different conditions for the LPE of α-MoO_3 were reported, employing different solvents such as NMP,[52] various alcohols[14,53] and water/surfactant mixtures.[54,55] It is possible to predict the LPE suitability of a solvent by resorting to several models, such as by considering the surface tension compatibility and the Hildebrand parameters.[56] However the mostly used and reliable way is to apply the Hansen solubility parameter (HSP) theory, commonly employed in polymer chemistry to predict the solubility, but demonstrated to work well also for LPE 2D materials.[56–59] The HSP theory states that the smaller is the interaction radius between the material and the solvent, the better will be the stability (Eq. 1):[60]

$$R_a = \sqrt{4(\delta_{d2} - \delta_{d1}) + \left(\delta_{p2} - \delta_{p1}\right) + (\delta_{h2} - \delta_{h1})} \quad \text{(Eq. 1)}$$

Where δ_{d2} is the dispersive component for the material chosen, δ_{d1} the dispersive component for the solvent, δ_{p2} and δ_{p1} the polar components for the material and the solvent respectively and δ_{h2} and δ_{h1} the hydrogen bonding part of the two.

Therefore, in order to minimize the Ra value and then increase the compatibility between a solvent and a material, the dispersive, polar and hydrogen-bonding parameters has to be as close as possible to each other. Based on this theory, in this work a pre-screening of different solvents was performed to ascertain the relative α-MoO_3 compatibility and determine which solvent should perform better. Among the examined solvents, water, a mixture of isopropanol (IPA) and water, acetone and butanone were selected. The first one was chosen mainly for its absence of toxicity and to test the possibility to exfoliate α-MoO_3 directly in water without the use of any surfactant, while the other ones were chosen because of low R_a ratio, with 2-butanone being the most promising one (see Table 1 for a summary of the HSPs for the here investigated solvents and for α-MoO_3, as well as the calculated Ra values).

Table 1. Hansen Solubility Parameters for the different solvent used in this work and for α-MoO_3 and relative Ra calculated between each solvent and the oxide employing Eq. 1

Solvent/material	$\boldsymbol{\delta_p}$	$\boldsymbol{\delta_d}$	$\boldsymbol{\delta_h}$	**Ra**
H_2O	18.1	17.1	16.9	13.8
IPA/H_2O (6:4 v/v)	16.7	10.5	16.6	10.6
2-butanone	16	9	5.1	4.0
acetone	15.5	10.4	7	5.2
α-MoO_3	17.8	8	6.5	/

In addition to varying the liquid medium, also the type of instrument (either SM or TS) and the exfoliation time (2, 4, 8 h) were tuned, to perform a systematic study and identify the optimal conditions for the LPE of α-MoO_3. Figure 1 summarizes the overall process and different conditions applied: powder bulk α-MoO_3 produced via hydrothermal synthesis[46] dispersed in the selected liquid media undergoes LPE in the different established conditions and the final mixture after exfoliation is subjected to multiple steps of liquid cascade centrifugation at increasing speed to selectively precipitate the non-exfoliated products (pellets) before obtaining a final colloidal ink of the most exfoliated α-MoO_3 material, used for further characterizations (see experimental details of this process in the methods section).

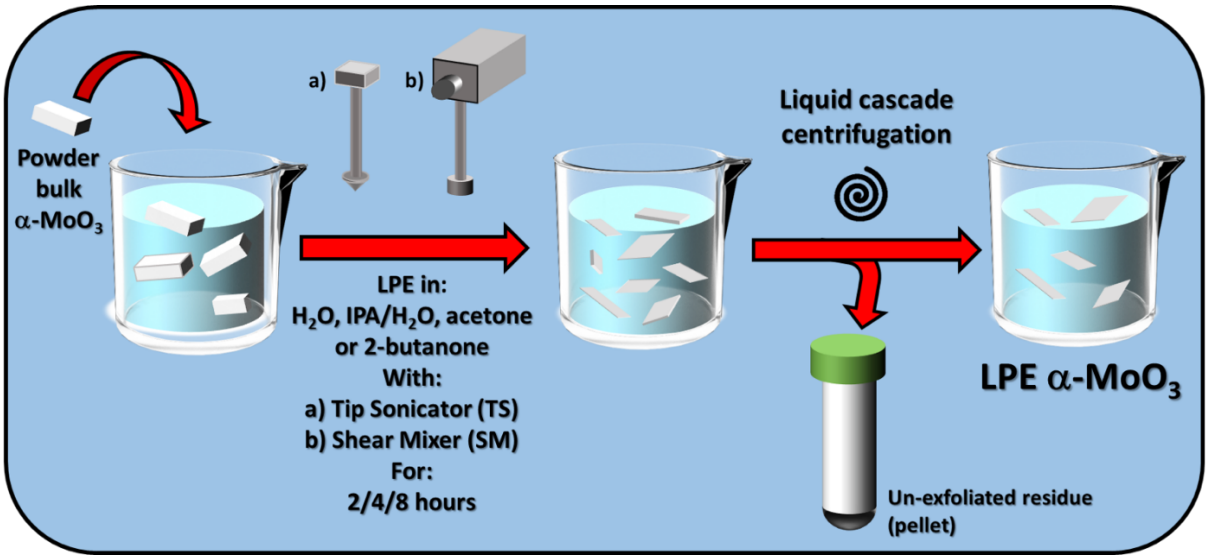

Figure 1. Schematic representation of the LPE process for α-MoO_3 described in this work and parameters whose effect was investigated, namely type of exfoliating instrument, liquid medium and exfoliation time.

Table 2 summarizes different data obtained for the various prepared LPE inks. By first looking only at the final colloid concentrations, it is possible to highlight different trends in relation to the instrument and solvent employed. For the samples exfoliated in water, shorter LPE times resulted to be more suitable in yielding higher concentration inks. For the ketones (acetone, 2-butanone) instead, the final ink concentrations increase with LPE time for almost all samples; however, this concentration is always lower compared to that obtained for the water exfoliated sample (for certain samples in 2-butanone, the concentration was too low to be effectively measured by weighting the dried residue). These values should be compared to other literature data: Hanlon et al.[52] reported an optimal yield of 0.17 mg/mL for LPE α-MoO_3 in pure IPA, while Dutta et al.[53] reported a yield of 0.33 mg/mL in ethanol/water. These numbers appear to be in perfect agreement with the order of magnitudes for LPE yield found by us, with some of ours even exceeding them slightly (for example SM H_2O).

Zeta potential (ZP) data, also summarized in Table 2, allow to estimate the colloidal stability of each final LPE MoO_3 ink. By examining them, it is possible to state a good match with the HSP theory used to actually select the liquid media. Indeed, ZP for 2-butanone and acetone suspensions have the highest values, between -30 and -45 mV, indicating long-term stable colloids, while ZP values for water are in the range between -25 and -40 mV, indicating a medium/short-term stability and those in IPA/water have values lower than -20 mV, hinting at relatively low-stability colloids prone to coagulation in a shorter timeframe.

Table 2. Summary of the different LPE α-MoO_3 inks, exfoliation time, employed instrument and relative concentrations, zeta potentials and E_{gap}.

Solvent 1 (v/v)	Solvent 2 (v/v)	LPE Time	LPE Method	Concentration (mg ml^{-1})	ZP[a] (meV)	E_{gap}[b] (eV)
H_2O	/	2 h	TS	0.27	-39 ± 1.2	3.62
H_2O	/	4 h	TS	0.34	-34 ± 2.1	3.64
H_2O	/	8 h	TS	0.24	-36 ± 1.6	3.68
IPA (6)	H_2O (4)	2 h	TS	0.36	-19 ± 2.9	3.07
IPA (6)	H_2O (4)	4 h	TS	0.24	-16 ±0.9	3.05
IPA (6)	H_2O (4)	8 h	TS	0.13	-9 ±0.6	3.05
2-butanone	/	2 h	TS	/	-42 ± 8.5	2.90
2-butanone	/	4 h	TS	0.015	-47 ± 0.8	3.00
2-butanone	/	8 h	TS	0.045	-42 ± 2.8	3.17
acetone	/	2 h	TS	0.06	-30 ± 2.1	3.06
acetone	/	4 h	TS	0.015	-35 ± 1.5	3.04
acetone	/	8 h	TS	0.045	-49 ± 1.9	2.97
H_2O	/	2 h	SM	0.57	-43 ±3.4	3.60
H_2O	/	4 h	SM	0.47	-27 ± 1.7	3.61
H_2O	/	8 h	SM	0.40	-32 ±1.6	3.65
IPA (6)	H_2O (4)	2 h	SM	0.19	-16 ± 1.0	3.05
IPA (6)	H_2O (4)	4 h	SM	0.21	-15 ± 0.3	3.06
IPA (6)	H_2O (4)	8 h	SM	0.19	-11 ± 0.7	3.07
2-butanone	/	2 h	SM	/	-33 ± 1.6	3.05
2-butanone	/	4 h	SM	/	-37 ± 1.7	3.09
2-butanone	/	8 h	SM	/	-31 ± 0.6	3.12
acetone	/	2 h	SM	0.02	-31 ± 0.4	3.00
acetone	/	4 h	SM	0.02	-15 ± 0.5	2.99
acetone	/	8 h	SM	0.07	-25 ± 0.6	3.00

[a] Values here reported are an average of three different measurements. [b] Calculated from the Tauc Plot derived from UV-Vis absorption spectra reported in Figure 2.

In order to characterize further the obtained LPE α-MoO_3 colloids, we carried out additional analyses, namely Raman and UV-Vis absorption spectroscopy and TEM/AFM. Raman scattering is widely employed to ascertain changes into phonon modes when a dimensional reduction is carried in a layered material progressing from the pure 3D to the 2D form. In many 2D materials such as MoS_2,[61,62] WS_2[63] and graphene[64,65] Raman spectroscopy has demonstrated to be one of the most powerful tools to state the number of layers present in a sample. However,

for the characterization of layered MoO_3, this technique does not provide significant information to distinguish the 2D form from the bulk. A comparison between the bulk α-MoO_3 powder Raman spectra and those of some representative exfoliated samples is reported in Figure S1 of the Supporting Information (S.I.). In these spectra, the signals at 996, at 666 cm^{-1} and at wavenumbers < 400 cm^{-1} show a slight red shift following dimensional reduction, which could be however within the Raman error, although it has been theoretically predicted[45] (the attribution of the signals to the different Raman modes is clarified in Table S1). Normalization on the most intense symmetric stretching mode of the terminal oxygen atoms or the doubly connected bridge–oxygen Mo–O–Mo at 818 cm^{-1} does not also highlight any change in relative intensity ratios with other modes, thus confirming that Raman for this specific layered material is not the suitable technique to ascertain the dimensional reduction, as it was shown before.[13,66] UV-Vis absorption spectra were acquired for all the LPE α-MoO_3 colloidal inks, as summarized in Figure 2, to verify whether a change in the energy of optical band gap (E_{gap}) of the α-MoO_3 can be detected following exfoliation, applying the Tauc method[46,67] to calculate its value at the absorption onset (all E_{gap} values are reported in Table 1).

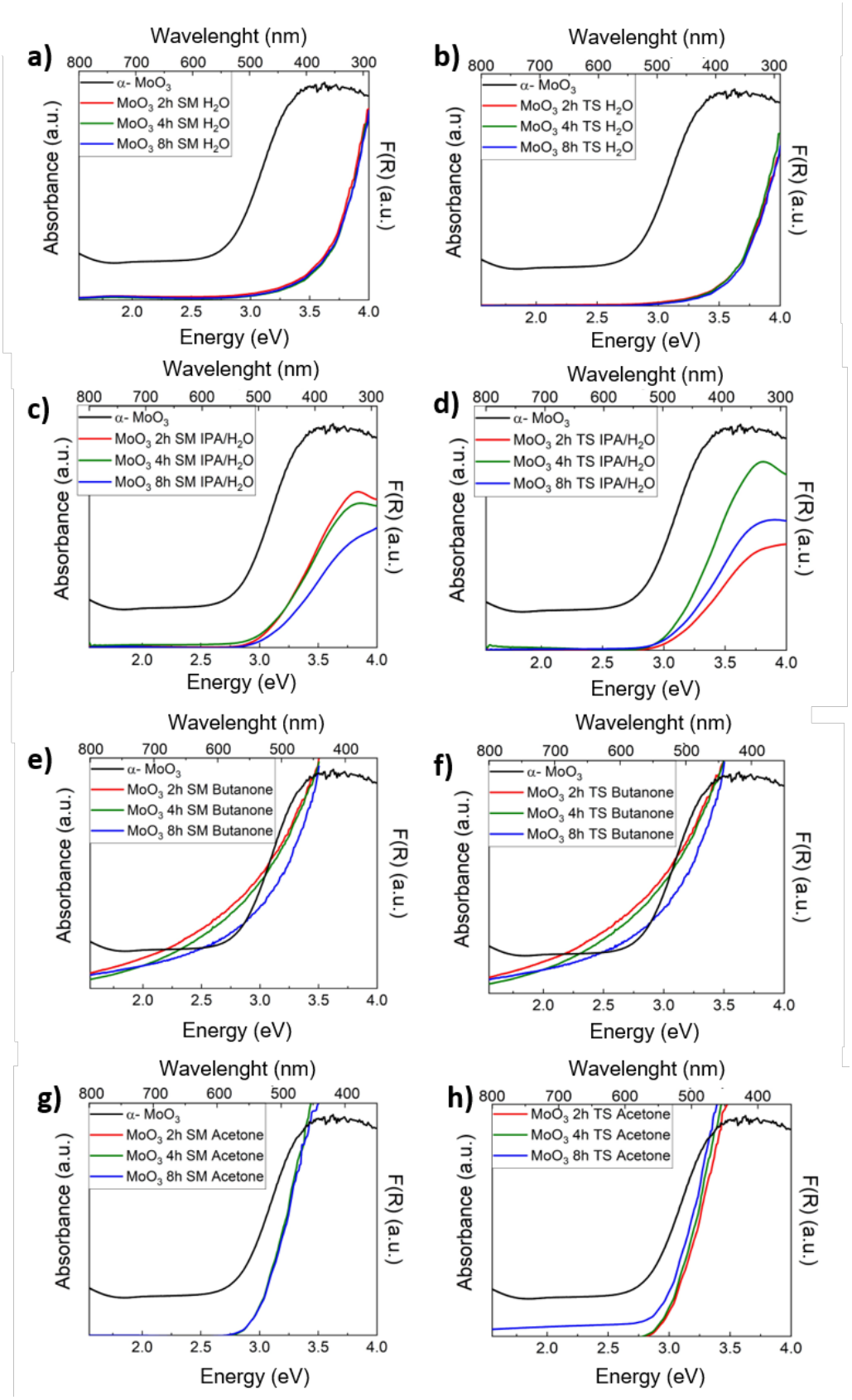

Figure 2. a-h) UV-Vis absorption spectra of the different LPE α-MoO_3 inks produced in this work employing multiple liquid media and SM or TS as the mechanical exfoliation method.

The spectrum of bulk α-MoO_3 was measured on the solid powder through reflectance spectroscopy and it is reported in every graph for the sake of comparison.

In TMDCs, this technique normally allows to follow the blue shift of the excitonic transition during exfoliation, in agreement with the quantum confinement effect;[68,69] however, α-MoO_3 does not present any excitonic absorption whose position can be probed by UV-Vis. Despite that, UV-Vis can still be used to determine the band gap and its shift. The as-synthesized bulk α-MoO_3 has a measured indirect band gap of 2.8 eV while all the LPE suspensions show an increase in this value from hundreds of meV up to almost 1 eV (Table 1). This indicates that possibly some samples might have undergone a dimensional reduction (for example the samples in pure H_2O, Figure 2a-b), while others might feature a quasi-2D structure (such as those in butanone, Figure 2e-f), as also previously reported in the literature.[70] To further investigate the variation in the electronic properties of α-MoO_3 following LPE, KPFM was performed to probe the work function (WF) of the material. KPFM data on the samples with the largest optical band gap (colloids in H_2O and IPA/H_2O) show an average value for the WF of 4.56 ± 0.56 eV, which appears to be decreased as compared to the values obtained from the bulk material,[46] i.e. 5.11 ± 0.50 eV, indicating a shift of the Fermi level towards the vacuum level, as expected following quantum confinement towards the 2D form.[71]

Despite the wide band gap of some of the prepared LPE α-MoO_3 inks (namely the ones in pure H_2O and IPA/H_2O mixture), remarkable changes in the color to the naked eye result depending on both solvent and instrument employed for the LPE. Figure 3a shows the two significant cases of the inks produced in IPA/H_2O via TS and in H_2O via SM, respectively: while the latter is a transparent, in line with the expectations considering the band gap of the material, the former presents a blue coloration. Since no significant traces of an absorption in the red zone of the visible spectrum are detected in the optical absorption spectra (Figure 2d), we expect that this coloration might be due to the presence of a relatively low quantity of Mo(V) moieties/oxygen vacancies, which can anyway contribute to change drastically the color of the ink.[72,73] In order to state the presence of Mo(V) in the blue-shaded ink, XPS measurements were performed (spectra of the molybdenum zone are reported in Figure 3b-d). From the XPS analysis it is possible to clearly highlight that in the bulk α-MoO_3 material some Mo(V) moieties were already present (Figure 3b). However, after LPE with the two different exfoliating devices (SM or TS), the quantity of Mo(V) sites slightly increases in the SM experiment (Figure 3c), but their concentration is perhaps not high enough to show their typical coloration in the resulting colloid. On the contrary, in the TS case (Figure 3d) a considerable increase in Mo(V) contribution in the photoemission spectrum is detected, thus explaining unambiguously the blue

color of the suspension. Such an increase in the number of defect sites is most likely related to the harsher LPE conditions that result from the use of the TS method, known to cause flakes breaking other than exfoliation only,[74,75] compared to the milder SM. It is particularly interesting to notice that such a blue coloration emerges as a predominant effect only at very high quantities of Mo(V) moieties in the materials, meaning that the nanostructures in suspensions can withstand a high degree of Mo(V) atoms (or oxygen vacancies). In addition, the coloration results more intense in alcohol-based mixtures: this can be explained by the slightly reducing character of the alcohol that likely promoted the formation of reduced species[76,77] during the exfoliation process (this phenomenon seems to increase when the samples are left in light, which might trigger the further Mo(VI) reduction by means of IPA).

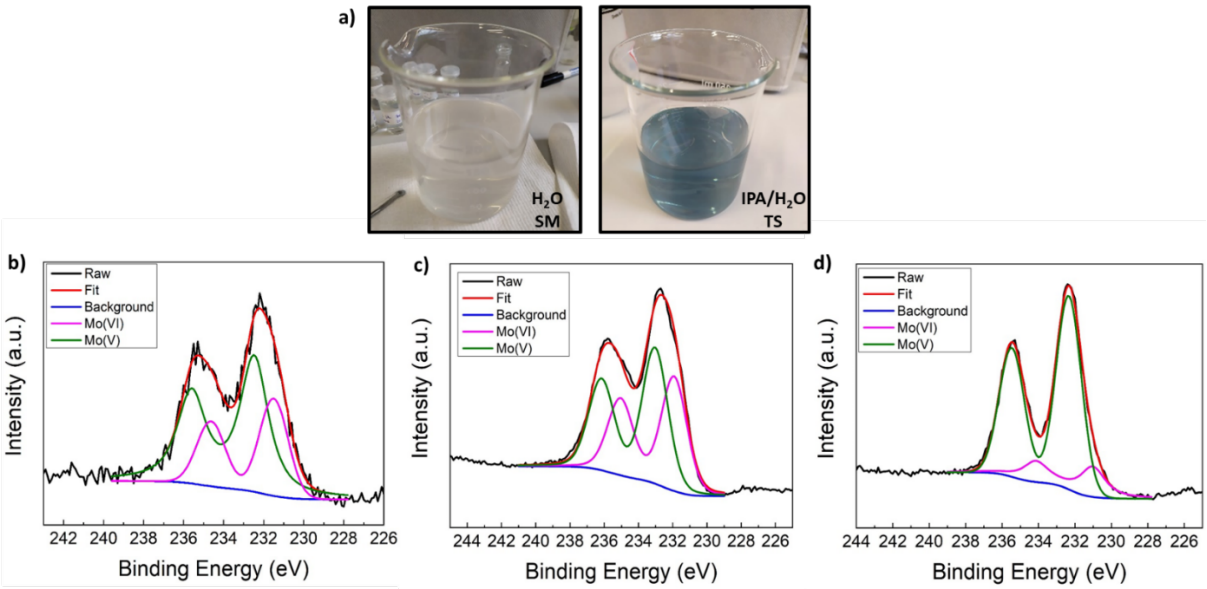

Figure 3. a) Pictures of the LPE α-MoO_3 colloids in pure H_2O prepared *via* SM (left) and IPA/H_2O prepared *via* TS (right). XPS analysis of b) as synthesized α-MoO_3 powder, c) LPE MoO_3 in H_2O prepared *via* SM and d) LPE MoO_3 in IPA/H_2O prepared *via* TS.

To compare the variation in electronic properties studied through UV-vis absorption with the effective nanomorphology of the resulting LPE α-MoO_3 colloids, HR-TEM analysis was performed to understand the size and dimension of the particles in suspension. Representative ink samples were selected to perform this analysis (see Figure 4 and Figure S2), based on their higher concentration with respect to other inks and optical band-gap opening (either large or small). From the TEM images, it can be seen that the sheet lateral size can reach dimensions up to 1 μm and that the material has been successfully exfoliated in some samples (see Figure 4a-b), especially in the H_2O LPE samples, which are also those reporting the highest opening of the optical band gap (Table 2). From a closer look at the images at high magnifications from

Figure 4, it is possible to highlight the atomic morphology of the nanosheets planes: particularly in Figure 4a, showing the aspect of the LPE samples in H_2O, atomic order appears to be altered compared to what should be expected from the starting crystalline α-MoO_3, hinting at a partial loss in crystallinity after LPE and at the concomitant formation of an amorphous phase in certain zones of the 2D nanosheets. Also, in the IPA/H_2O ink, this amorphous phase seems to be partially present (Figure 4b), together with crystalline domains, pointing at an amorphization of the material in the presence of water during LPE. On the other hand, the TEM images of the LPE sample in butanone (Figure S2) clearly show that the low E_{gap} increase with respect to the bulk α-MoO_3 is due to a non-efficient production of few-layered species. The presence of an amorphous component can be further detected by carrying out P-XRD analysis of the LPE α-MoO_3 dried material: Figure S3 show a comparison between the diffractograms of bulk α-MoO_3 and of the exfoliated samples in H_2O (SM 8 h) and in IPA/H_2O (TS 4 h), from which, in the two latter samples, the emergence of the typical α-MoO_3 reflexes from a large amorphous background is clearly detected which is not present at all in the former. On the other hand, SAED analysis carried out locally on individual nanosheets on the TEM grid shows the presence of crystalline features (Figure S4), although these reflexes are coincident with high 2θ value reflexes in the P-XRD patterns of α-MoO_3, while the main material reflexes remain buried in the central part of the SAED pattern and thus are not distinguishable.

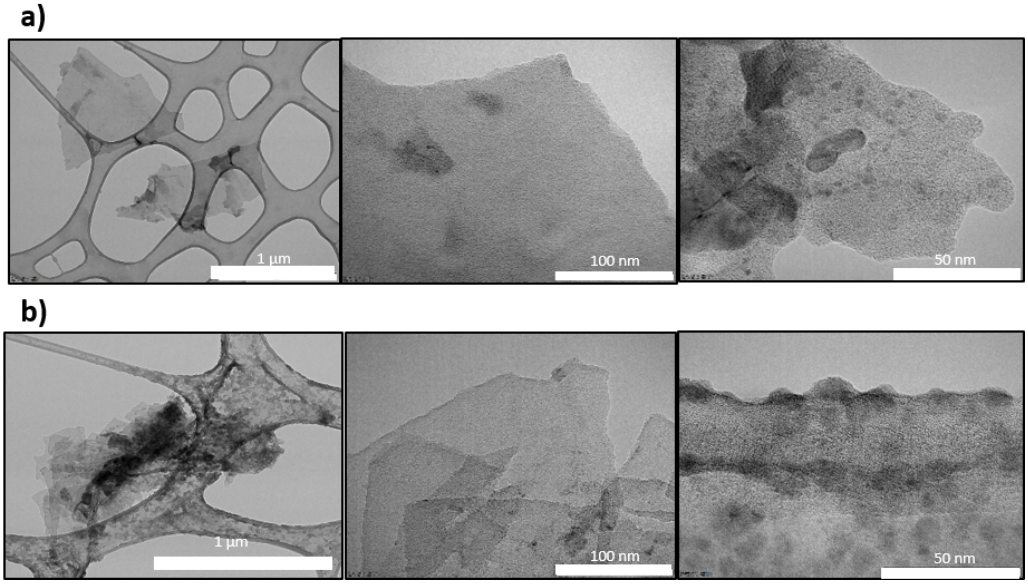

Figure 4. HR-TEM images of representative LPE α-MoO_3 colloids. a) Samples in H_2O obtained *via* SM for 8 h and b) samples in IPA/H_2O obtained *via* TS for 4 h.

Once the information about the dimension and morphology of the LPE materials was obtained through TEM, the investigation was focused on understanding the thickness of the nanosheets,

and to this aim atomic force microscopy (AFM) analysis was performed (results are displayed in Figure S5 in the S.I.). Through this analysis, it was possible to track nanosheet thicknesses varying within a narrow range, from bilayers (≈ 1.8 nm) to 5-6 layers (≈ 5-6 nm), further demonstrating that in the case of the colloidal samples in H_2O and IPA/H_2O the LPE was successful.

To gain further insights into the atomic arrangement of the obtained LPE α-MoO_3 colloids produced via LPE in different liquid media, XAS measurements were performed at the SAMBA beamline of the SOLEIL synchrotron (Gif-sur-Yvette, France) directly on the colloidal inks and on the solid material obtained after drying the ink in H_2O produced *via* SM, being this one the most promising in term of 2D aspect ratio, and the results were compared to those obtained for the α-MoO_3 precursor in solid form and also for the precursor of this last one, namely ammonium heptamolybdate (AHM). Next, the XANES spectra are first discussed, allowing to unravel the atomic configuration around the Mo atoms, i.e. their coordination sphere in the 2D nanosheets as compared to the bulk material. The recorded spectra are shown in Figure 5 for both the colloidal inks and the dried powder, in comparison with the α-MoO_3 precursor and AHM, being both these references known to feature an octahedral coordination geometry around the Mo atoms. The liquid suspensions in Figure 5a show features similar to those of bulk α-MoO_3, in particular a pre-edge feature at around 20.07 keV representing the forbidden 1s→4d transition in Mo atoms.[78] This transition becomes more pronounced when there is an overlap between O p-orbitals and Mo d-orbitals, with a high degree of distortion greatly improving such overlap and subsequently the intensity of the pre-edge feature. By comparing this peak across the different samples, it is possible to evidence that those obtained by LPE in H_2O and IPA/H_2O show a less intense pre-edge feature, indicating the existence of a higher symmetry compared to the reference compounds α-MoO_3 and AHM, while that in butanone gives rise to a more intense signal in the same zone, indicating a more distorted structure. By analyzing the main edge feature, information on the type of Mo site can be gathered: in general, octahedrally coordinated Mo features 3 main peaks, indicated in Figure 5 as A (20.025 keV), B (20.037 keV) and C (20.055 keV). These originate from MoO_6 octahedra (a structure composed of four long Mo-O bond and two shorter Mo=O bonds) sharing edges, and their relative intensity differs depending on different Mo sites present in these polyoxoanion structures.[79] These sites are called 1, 1' and 2: the first two represent a Mo atom sharing the edges with three other Mo atoms, with a slightly difference in Mo-O bond length, while the site 2 represents a Mo atom surrounded by 6 MoO_6 octahedra.[79] For this latter site in particular, the intensity of peak B is much less intense as compared to sites 1 and 1'. Specifically, in the spectra presented here it is possible to notice how the LPE samples in H_2O feature an increase in intensity and

small shift towards lower energy in peak B, in direct relation to the absence of type 2 sites, and a decrease in intensity in peak C, which is connected both to the Mo coordination but also to the second O shell around Mo. Those two variations altogether account for a decrease of type 2 sites and a decrease in long range interactions between different Mo and O, which can be related to a decrease in dimensionality. In addition, this sample also show a slight shift of the absorption edge position towards lower energies, compatible with the presence of the Mo(V) moieties detected *via* XPS. The presence of these reduced species has an even more profound effect on the sample in IPA/H2O prepared via TS, since the edge position is also shifted but, more relevantly, feature B is strongly shifted and overlaps with peak A.

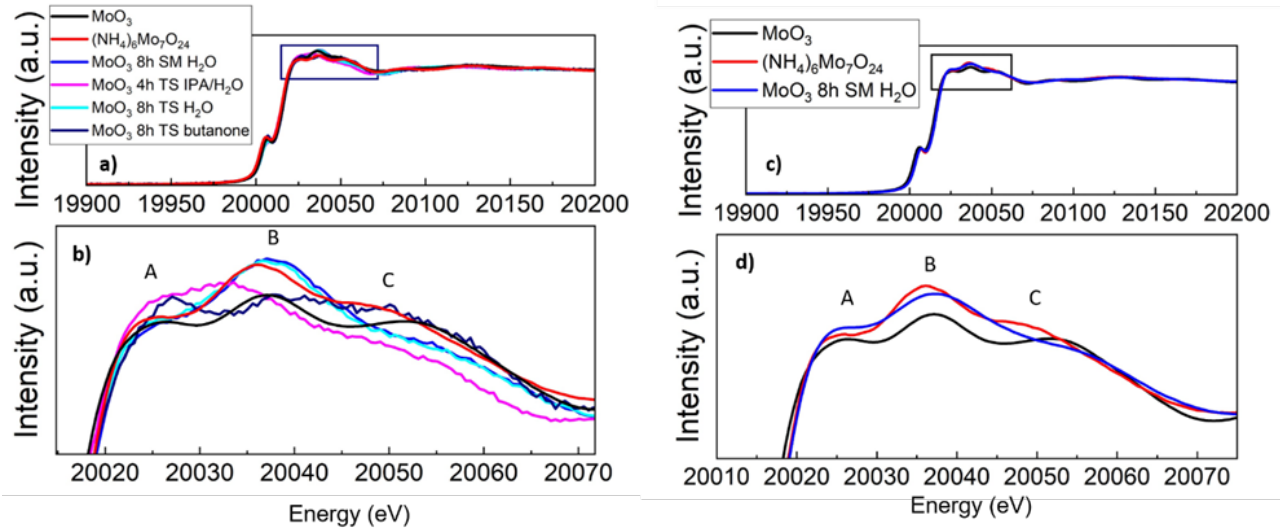

Figure 5. XANES spectra of a) LPE α-MoO_3 colloidal inks with b) relative zoom in the post-Mo-edge features. c) XANES spectra of LPE α-MoO_3 powder obtained after drying the ink produced in H_2O after 8 h SM with relative zoom on the post-Mo-edge features in d). In all the spectra, also an internal comparison with the spectra of the precursors α-MoO_3 and AHM are reported (measured as powders) for the sake of comparison.

Comparison has to be made then with the XANES spectra of a dried powder obtained from the best 2D colloid available among the here analyzed (namely the H_2O 8h SM, Figure 5d), where it is possible to observe, upon drying, a clear change in the spectrum: the pre-edge and edge features resemble those in the AHM spectra, rather than the α-MoO_3, indicating distorted octahedra around the Mo(VI) centers. Compared to the crystalline α-MoO_3, peak A slightly increases in intensity, while peak C decreases: those combined observations suggest a change in ratio between site 1 and 1' (see the different computed site contributions in Figure S6), overall pointing to a partial restacking of the 2D nanosheets once they are not anymore in the colloidal state.

The extended X-ray absorption fine structure (EXAFS) part of the XAS spectrum was further analyzed for the dry sample (for the inks this was not possible given the too low signal to noise ratio). This analysis provides information about bond lengths around the scattering atom and changes in those lengths are detected for the here investigated materials when going from bulk α-MoO_3 to the 2D MoO_3 nanosheets (see Figure 6 and Table S2 in the S.I. for a list of the estimated bond lengths). While the first coordination shell resulted similar to the bulk oxide in terms of Mo-O lengths, in the second coordination sphere both Mo-O and Mo-Mo bonds are considerably shorter in the 2D LPE α-MoO_3 powder compared to the bulk material. A similar effect can be attributed to a certain strain existing within the 2D nanosheets, as evidenced previously also for TMDs,[80] and provides new interesting insights into the structure of few-layers α-MoO_3 which can have an effect on the optical and electronic properties of this low-dimensional material, as it has been highlighted previously for 2D TMDs.[81]

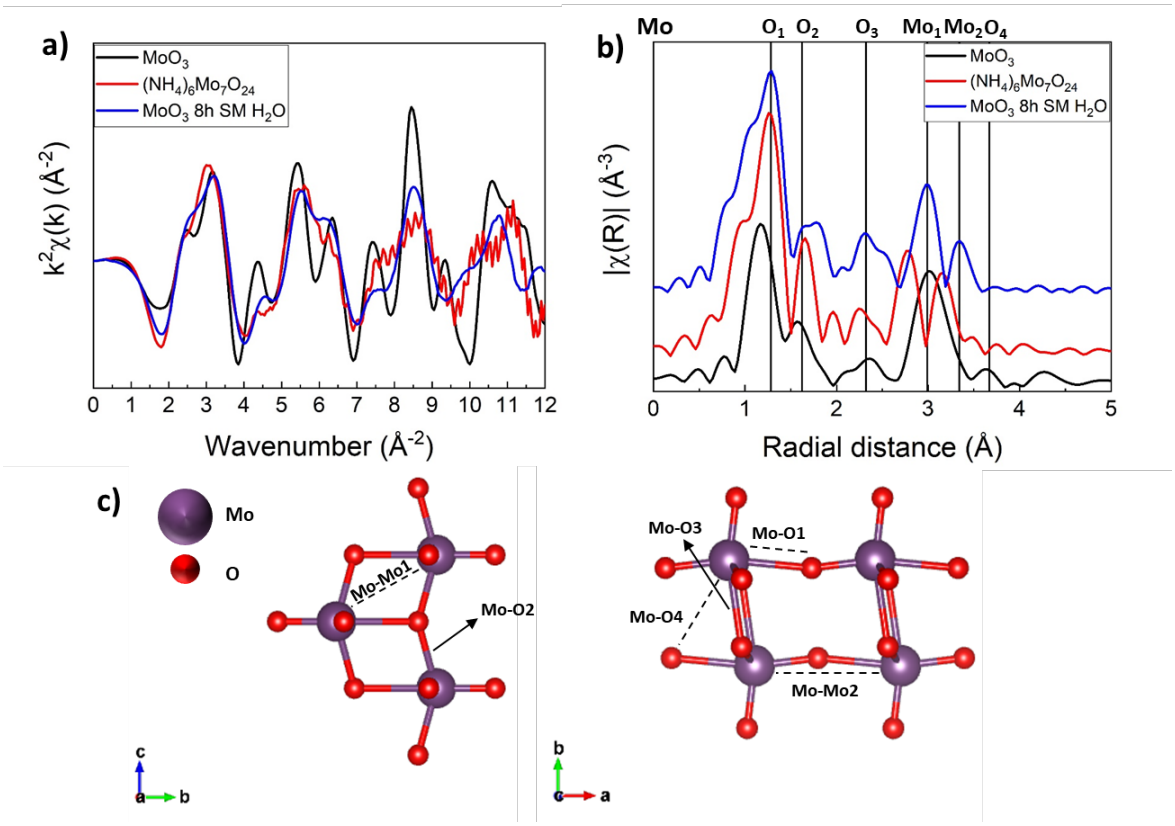

Figure 6. a) EXAFS spectra and b) not-corrected Fourier Transformed EXAFS spectra of LPE α-MoO_3 powder obtained after drying the ink in H_2O prepared through 8h SM. The internal comparison with the spectra of the precursors α-MoO_3 and AHM is also reported. c) Details of the α-MoO_3 crystal structure highlighting the atomic distances probed by the EXAFS analysis (left: view along the a-axis; right: view along the c-axis).

To gain deeper insight into the experimental data, computational analyses on the 3D bulk structure of α-MoO_3 and the 2D slab were performed, and the results are reported in Figure 7. After geometry optimization of both bulk and slab structures, very similar bond length as measured by EXAFS were obtained, with a maximum error of 0.23 Å for the Mo-O1 distance in the bulk and of 0.62 Å for the Mo-O3 distance in the slab. Since this bond distance is in the direction of the vacuum in the slab, it should not strongly affect the electronic properties here reported. Interestingly, we observe only slight variation in the DOS going from bulk to slab, with a main decrease in intensity rather than energy position. Yet, a band opening of around 50 meV was obtained at the Gamma point, from a value of 2.79 eV for the bulk to 2.85 eV for the slab. The bandgap opening in is excellent agreement with the measured UV data. The discrepancy between some experimental values and the computation arises from two factors, namely that all the calculations were performed in vacuum, for a single layer structure, and without considering the effect of the different solvents on the electronic properties. Nevertheless, a large shift in the work function value has been computed, with value of 5.36 and 4.96 eV going from bulk to slab, which is again in excellent agreement with the measured values, and suggests a shift towards the vacuum for the slab, as well as the low importance of the solvent nature in determining the electronic properties of the slab (the solvent is important for LPE, but does not affect the gap or WF shift). This is directly related to the quantum confinement effect which rises when the dimensionality of a system is decreased, thus shifting the Fermi level towards the vacuum.[71]

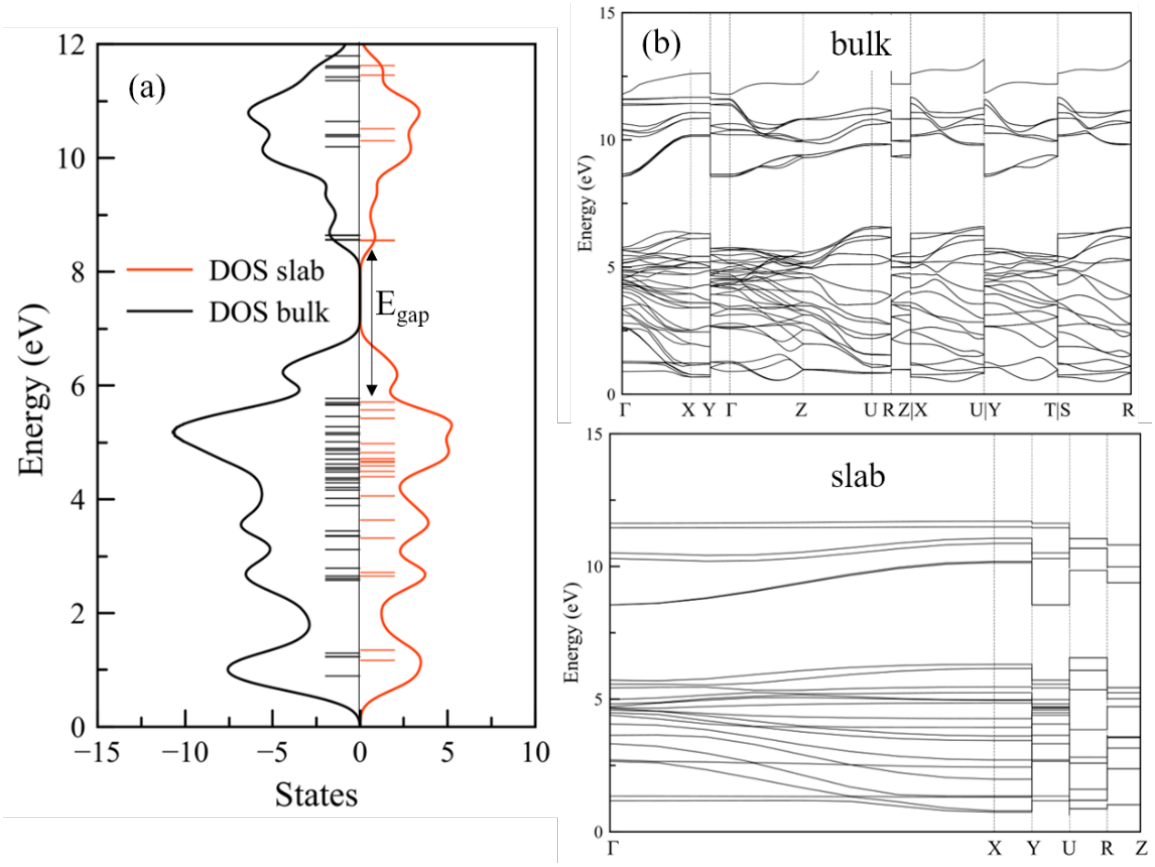

Figure 7. a) Total density of states for the bulk (black line) and slab (red line) of α-MoO_3. The horizontal lines refer to the eigenvalues. b) band structure along the first Brillouin zone for both bulk and slab α-MoO_3.

3. Conclusions

In this work, we describe a detailed analysis of the LPE process for the layered oxide α-MoO_3, a wide band gap semiconducting material that is attracting increasing attention for a variety of functional purposes, ranging from (opto)electronics to electrochromism, energy storage and catalysis.[45] Considering such attention that is progressively receiving by the scientific community active in the field of 2D materials research, it is timely to provide a comprehensive study as the present one, in which the parameters for the efficient LPE of α-MoO_3 targeting the production of its 2D colloids in low-environmental impact liquid media are thoroughly explored, allowing to identify the best operating conditions. The use of water-based solvents results to be the right condition to ensure the formation of few-layers nanosheets, correlated to an opening of the optical band gap and a shift in the Fermi level in direction of vacuum, being both electronic peculiarities of the dimensional reduction.[82] The yield in LPE 2D material is still relatively modest, but it could be improved by resorting to pre-treatments on the bulk α-MoO_3,

such as the pre-intercalation of water molecules followed by a series of freeze-thaw cycles that cause water freezing expansion, as it has been reported previously by Li et al.[83]

In parallel to this characterization, for the first time we report here the results of a XAS investigation that compares the bulk and 2D form of α-MoO_3, allowing to evidence extremely precise structural parameters at the atomic level. This points out at the potential of this technique to probe the local environment in 2D nanosheets, suggesting how this could be in the future more widely implemented also on other 2D materials to shine better light on structure-to-property relationships. Finally, through theoretical investigation, we strengthen the validity of the experimental results, effectively clarifying such relationships in the here analyzed α-MoO_3 with different dimensionalities.

This work will serve as a valuable tool in the hand of other investigators interested at applying 2D α-MoO_3 nanosheets in functional applications, resorting to this material as a colloidal ink, a pre-requisite for enabling in the future large-area processing and industrial scale implementation.[41]

Supporting information

Raman spectra and Raman modes assignment for LPE α-MoO_3; Absorption spectra of LPE α-MoO_3 thin films and SEM images of their cross-section; additional HR-TEM images and AFM analysis of LPE α-MoO_3; XRD and SAED spectra of LPE α-MoO_3; Bond distances and other parameters obtained from EXAFS spectra; comparison between experimental and calculated XANES spectra.

Acknowledgements

M.C. and T.G. acknowledge financial support from the European Commission through the H2020 FET-PROACTIVE-EIC-07-2020 project LIGHT-CAP (project number 101017821). S.O acknowledges the Polish National Agency for Academic Exchange under the Bekker program (grant no. PPN/BEK/2020/ 1/00053/U/00001). This research was carried out with the support of the Interdisciplinary Center for Mathematical and Computational Modeling at the University of Warsaw (ICM UW) under grant no G83-28. S.G., F.L. and M.C. acknowledge the "Centro Levi Cases" of the University of Padova for financial support (AMONRA project). S.G. gratefully thanks the Deutsche Forschungsgemeinschaft (DFG, German Research Foundation) – for funding a "Mercator Fellowship" position within the SFB 1441 – Project-ID 426888090 at KIT Karlsruhe and the DAAD for a visiting professorship (2021) at the Justus Liebig Universität Giessen. P.D. acknowledge support by the state of Baden-Württemberg through bwHPC and the DFG through grant no INST 40/575-1 FUGG (JUSTUS 2 cluster).

SOLEIL synchrotron facility is kindly acknowledged for provision of beamtime (Proposal 20201498). We thank Emiliano Fonda, SAMBA beamline scientist, for technical support during the remote beamtime.

References

(1) Gatti, T.; Lamberti, F.; Mazzaro, R.; Kriegel, I.; Schlettwein, D.; Enrichi, F.; Lago, N.; Maria, E. Di; Meneghesso, G.; Vomiero, A.; Gross, S. Opportunities from Doping of Non-Critical Metal Oxides in Last Generation Light-Conversion Devices. *Adv. Energy Mater.* **2021**, *11* (31), 2101041. https://doi.org/10.1002/AENM.202101041.

(2) Greiner, M. T.; Helander, M. G.; Tang, W. M.; Wang, Z. Bin; Qiu, J.; Lu, Z. H. Universal Energy-Level Alignment of Molecules on Metal Oxides. *Nat. Mater.* **2012**, *11* (1), 76–81. https://doi.org/10.1038/nmat3159.

(3) Greiner, M. T.; Lu, Z.-H. Thin-Film Metal Oxides in Organic Semiconductor Devices: Their Electronic Structures, Work Functions and Interfaces. *NPG Asia Mater. 2013 57* **2013**, *5* (7), e55–e55. https://doi.org/10.1038/am.2013.29.

(4) Meyer, J.; Hamwi, S.; Kröger, M.; Kowalsky, W.; Riedl, T.; Kahn, A. Transition Metal Oxides for Organic Electronics: Energetics, Device Physics and Applications. *Adv. Mater.* **2012**, *24* (40), 5408–5427. https://doi.org/10.1002/ADMA.201201630.

(5) Zhu, Y.; Yao, Y.; Luo, Z.; Pan, C.; Yang, J.; Fang, Y.; Deng, H.; Liu, C.; Tan, Q.; Liu, F.; Guo, Y. Nanostructured MoO3 for Efficient Energy and Environmental Catalysis. *Molecules* 2020. https://doi.org/10.3390/molecules25010018.

(6) Yu, X.; Marks, T. J.; Facchetti, A. Metal Oxides for Optoelectronic Applications. *Nat. Mater.* **2016**, *15* (4), 383–396. https://doi.org/10.1038/nmat4599.

(7) Guo, Y.; Robertson, J. Origin of the High Work Function and High Conductivity of MoO3. *Appl. Phys. Lett.* **2014**, *105* (22). https://doi.org/10.1063/1.4903538.

(8) Dixit, D.; Madhuri, K. V. Electrochromism in MoO3 Nanostructured Thin Films. *Superlattices Microstruct.* **2021**, *156*, 106936. https://doi.org/10.1016/J.SPMI.2021.106936.

(9) Novak, T. G.; Kim, J.; Tiwari, A. P.; Kim, J.; Lee, S.; Lee, J.; Jeon, S. 2D MoO3Nanosheets Synthesized by Exfoliation and Oxidation of MoS2for High Contrast and Fast Response Time Electrochromic Devices. *ACS Sustain. Chem. Eng.* **2020**, *8* (30), 11276–11282. https://doi.org/10.1021/acssuschemeng.0c03191.

(10) Arvizu, M. A.; Morales-Luna, · M; Pérez-González, · M; Campos-Gonzalez, · E; Zelaya-Angel, · O; Tomás, · S A; Arvizu, B. M. A.; Mx, M. C. Influence of Thermal Annealings in Argon on the Structural and Thermochromic Properties of MoO 3 Thin Films. *Int. J. Thermophys.* **2017**, *38*, 51. https://doi.org/10.1007/s10765-017-2190-1.

(11) Szkoda, M.; Trzciński, K.; Klein, M.; Siuzdak, K.; Lisowska-Oleksiak, A. The Influence of Photointercalaction and Photochromism Effects on the Photocatalytic Properties of Electrochemically Obtained Maze-like MoO3 Microstructures. *Sep. Purif. Technol.* **2018**, *197*, 382–387. https://doi.org/10.1016/J.SEPPUR.2018.01.033.

(12) Ma, Y. T.; Ma, S. Y.; Tang, J.; Wu, Z. G.; Shi, J.; Zhao, Y.; Wang, Y.; Pei, S. T. Constructed Heterostructured SnS@MoO3 Hollow Nanotubes and Detected Sensing Properties towards TEA. *Vacuum* **2021**, *184*. https://doi.org/10.1016/j.vacuum.2020.109939.

(13) Datta, R. S.; Haque, F.; Mohiuddin, M.; Carey, B. J.; Syed, N.; Zavabeti, A.; Zhang, B.; Khan, H.; Berean, K. J.; Ou, J. Z.; Mahmood, N.; Daeneke, T.; Kalantar-Zadeh, K. Highly Active Two Dimensional α-MoO3-: X for the Electrocatalytic Hydrogen Evolution Reaction. *J. Mater. Chem. A* **2017**, *5* (46), 24223–24231. https://doi.org/10.1039/c7ta07705j.

(14) Zhang, H.; Gao, L.; Gong, Y. Exfoliated MoO3 Nanosheets for High-Capacity Lithium Storage. *Electrochem. commun.* **2015**, *52*, 67–70. https://doi.org/10.1016/j.elecom.2015.01.014.

(15) Zhu, K.; Wang, X.; Liu, J.; Li, S.; Wang, H.; Yang, L.; Liu, S.; Xie, T. Novel Amorphous MoS2/MoO3/Nitrogen-Doped Carbon Composite with Excellent Electrochemical Performance for Lithium Ion Batteries and Sodium Ion Batteries. *ACS Sustain. Chem. Eng.* **2017**, *5* (9), 8025–8034. https://doi.org/10.1021/ACSSUSCHEMENG.7B01595.

(16) Razmyar, S.; Sheng, T.; Akter, M.; Zhang, H. Lowerature Photocatalytic Hydrogen Addition to Two-Dimensional MoO3 Nanoflakes from Isopropyl Alcohol for Enhancing Solar Energy Harvesting and Conversion. *ACS Appl. Nano Mater.* **2019**, *2* (7), 4180–4192. https://doi.org/10.1021/acsanm.9b00645.

(17) Avigad, E.; Etgar, L. Studying the Effect of MoO3 in Hole-Conductor-Free Perovskite Solar Cells. *ACS Energy Lett.* **2018**, *3* (9), 2240–2245. https://doi.org/10.1021/ACSENERGYLETT.8B01169.

(18) de Castro, I. A.; Datta, R. S.; Ou, J. Z.; Castellanos-Gomez, A.; Sriram, S.; Daeneke, T.; Kalantar-zadeh, K. Molybdenum Oxides – From Fundamentals to Functionality. *Advanced Materials*. Wiley-VCH Verlag October 2017. https://doi.org/10.1002/adma.201701619.

(19) Ren, H.; Sun, S.; Cui, J.; Li, X. Synthesis, Functional Modifications, and Diversified Applications of Molybdenum Oxides Micro-/Nanocrystals: A Review. *Cryst. Growth Des.* **2018**, *18* (10), 6326–6369. https://doi.org/10.1021/acs.cgd.8b00894.

(20) Manzeli, S.; Ovchinnikov, D.; Pasquier, D.; Yazyev, O. V.; Kis, A. 2D Transition Metal Dichalcogenides. *Nat. Rev. Mater. 2017 28* **2017**, *2* (8), 1–15. https://doi.org/10.1038/natrevmats.2017.33.

(21) Kumbhakar, P.; Chowde Gowda, C.; Mahapatra, P. L.; Mukherjee, M.; Malviya, K. D.; Chaker, M.; Chandra, A.; Lahiri, B.; Ajayan, P. M.; Jariwala, D.; Singh, A.; Tiwary, C. S. Emerging 2D Metal Oxides and Their Applications. *Mater. Today* **2021**, *45*, 142–168. https://doi.org/10.1016/J.MATTOD.2020.11.023.

(22) Guan, M.; Wang, Q.; Zhang, X.; Bao, J.; Gong, X.; Liu, Y. Two-Dimensional Transition Metal Oxide and Hydroxide-Based Hierarchical Architectures for Advanced Supercapacitor Materials. *Front. Chem.* **2020**, *0*, 390. https://doi.org/10.3389/FCHEM.2020.00390.

(23) Browne, M. P.; Sofer, Z.; Pumera, M. Layered and Two Dimensional Metal Oxides for Electrochemical Energy Conversion. *Energy Environ. Sci.* **2019**, *12* (1), 41–58. https://doi.org/10.1039/C8EE02495B.

(24) Timmerman, M. A.; Xia, R.; Le, P. T. P.; Wang, Y.; Elshof, J. E. ten. Metal Oxide Nanosheets as 2D Building Blocks for the Design of Novel Materials. *Chem. – A Eur. J.* **2020**, *26* (42), 9084–9098. https://doi.org/10.1002/CHEM.201905735.

(25) Hernandez, Y.; Nicolosi, V.; Lotya, M.; Blighe, F. M.; Sun, Z.; De, S.; McGovern, I. T.; Holland, B.; Byrne, M.; Gun'Ko, Y. K.; Boland, J. J.; Niraj, P.; Duesberg, G.; Krishnamurthy, S.; Goodhue, R.; Hutchison, J.; Scardaci, V.; Ferrari, A. C.; Coleman, J. N. High-Yield Production of Graphene by Liquid-Phase Exfoliation of Graphite. *Nat. Nanotechnol.* **2008**, *3* (9), 563–568. https://doi.org/10.1038/nnano.2008.215.

(26) Hu, G.; Kang, J.; Ng, L. W. T.; Zhu, X.; Howe, R. C. T.; Jones, C. G.; Hersam, M. C.; Hasan, T. Functional Inks and Printing of Two-Dimensional Materials. *Chem. Soc. Rev.* **2018**, *47* (9), 3265–3300. https://doi.org/10.1039/C8CS00084K.

(27) Huang, Y.; Pan, Y. H.; Yang, R.; Bao, L. H.; Meng, L.; Luo, H. L.; Cai, Y. Q.; Liu, G. D.; Zhao, W. J.; Zhou, Z.; Wu, L. M.; Zhu, Z. L.; Huang, M.; Liu, L. W.; Liu, L.; Cheng, P.; Wu, K. H.; Tian, S. B.; Gu, C. Z.; Shi, Y. G.; Guo, Y. F.; Cheng, Z. G.; Hu, J. P.; Zhao, L.; Yang, G. H.; Sutter, E.; Sutter, P.; Wang, Y. L.; Ji, W.; Zhou, X. J.; Gao, H. J. Universal Mechanical Exfoliation of Large-Area 2D Crystals. *Nat. Commun.* **2020**, *11* (1), 1–9. https://doi.org/10.1038/s41467-020-16266-w.

(28) Backes, C.; Higgins, T. M.; Kelly, A.; Boland, C.; Harvey, A.; Hanlon, D.; Coleman, J. N. Guidelines for Exfoliation, Characterization and Processing of Layered Materials Produced by Liquid Exfoliation. *Chem. Mater.* **2017**, 243–255. https://doi.org/10.1021/acs.chemmater.6b03335.

(29) Blake, P.; Brimicombe, P. D.; Nair, R. R.; Booth, T. J.; Jiang, D.; Schedin, F.; Ponomarenko, L. A.; Morozov, S. V; Gleeson, H. F.; Hill, E. W.; Geim, A. K.; Novoselov, K. S. Graphene-Based Liquid Crystal Device. *Nano Lett.* **2008**, *8* (6), 1704–1708. https://doi.org/10.1021/nl080649i.

(30) Wang, H.; Su, X.; Song, T.; Li, Z.; Zhao, Y.; Lou, H.; Wang, J. Scalable Exfoliation and Dispersion of Few-Layer Hexagonal Boron Nitride Nanosheets in NMP-Salt Solutions. *Appl. Surf. Sci.* **2019**, *488*, 656–661. https://doi.org/10.1016/j.apsusc.2019.05.296.

(31) Gupta, A.; Arunachalam, V.; Vasudevan, S. Liquid-Phase Exfoliation of MoS2 Nanosheets: The Critical Role of Trace Water. *J. Phys. Chem. Lett.* **2016**, *7* (23), 4884–4890. https://doi.org/10.1021/acs.jpclett.6b02405.

(32) Han, G. Q.; Liu, Y. R.; Hu, W. H.; Dong, B.; Li, X.; Chai, Y. M.; Liu, Y. Q.; Liu, C. G. WS2 Nanosheets Based on Liquid Exfoliation as Effective Electrocatalysts for Hydrogen Evolution Reaction. *Mater. Chem. Phys.* **2015**, *167*, 271–277. https://doi.org/10.1016/J.MATCHEMPHYS.2015.10.043.

(33) Vacacela Gomez, C.; Guevara, M.; Tene, T.; Villamagua, L.; Usca, G. T.; Maldonado, F.; Tapia, C.; Cataldo, A.; Bellucci, S.; Caputi, L. S. The Liquid Exfoliation of Graphene in Polar Solvents. *Appl. Surf. Sci.* **2021**, *546*, 149046. https://doi.org/10.1016/J.APSUSC.2021.149046.

(34) Esfandiari, M.; Mohajerzadeh, S. Formation of Large Area WS2 Nanosheets Using an Oxygen-Plasma Assisted Exfoliation Suitable for Optical Devices. *Nanotechnology* **2019**, *30* (42), 425204. https://doi.org/10.1088/1361-6528/AB31B5.

(35) El Garah, M.; Bertolazzi, S.; Ippolito, S.; Eredia, M.; Janica, I.; Melinte, G.; Ersen, O.; Marletta, G.; Ciesielski, A.; Samorì, P. MoS2 Nanosheets via Electrochemical Lithium-Ion Intercalation under Ambient Conditions. *FlatChem* **2018**, *9*, 33–39. https://doi.org/10.1016/J.FLATC.2018.06.001.

(36) Hu, C.-X.; Shin, Y.; Read, O.; Casiraghi, C. Dispersant-Assisted Liquid-Phase Exfoliation of 2D Materials beyond Graphene. *Nanoscale* **2021**, *13* (2), 460–484. https://doi.org/10.1039/D0NR05514J.

(37) Vook, R. W. Theories Of Nucleation And Growth Of Thin Films. In *Thin Film Technologies and Special Applications*; Hunter, W. R., Ed.; SPIE, 1982; Vol. 0346, pp 2–8. https://doi.org/10.1117/12.933784.

(38) Paolucci, V.; D'Olimpio, G.; Lozzi, L.; Mio, A. M.; Ottaviano, L.; Nardone, M.; Nicotra, G.; Le-Cornec, P.; Cantalini, C.; Politano, A. Sustainable Liquid-Phase Exfoliation of Layered Materials with Nontoxic Polarclean Solvent. *ACS Sustain. Chem. Eng.* **2020**, *8* (51), 18830–18840. https://doi.org/10.1021/acssuschemeng.0c04191.

(39) Parvez, K.; Worsley, R.; Alieva, A.; Felten, A.; Casiraghi, C. Water-Based and Inkjet Printable Inks Made by Electrochemically Exfoliated Graphene. *Carbon* **2019**, *149*, 213–221. https://doi.org/10.1016/J.CARBON.2019.04.047.

(40) McManus, D.; Vranic, S.; Withers, F.; Sanchez-Romaguera, V.; Macucci, M.; Yang, H.; Sorrentino, R.; Parvez, K.; Son, S.-K.; Iannaccone, G.; Kostarelos, K.; Fiori, G.; Casiraghi, C. Water-Based and Biocompatible 2D Crystal Inks for All-Inkjet-Printed Heterostructures. *Nat. Nanotechnol.* **2017**, *12* (4), 343–350. https://doi.org/10.1038/nnano.2016.281.

(41) Guohua Hu; Joohoon Kang; T. Ng, L. W.; Xiaoxi Zhu; T. Howe, R. C.; G. Jones, C.; C. Hersam, M.; Tawfique Hasan. Functional Inks and Printing of Two-Dimensional Materials. *Chem. Soc. Rev.* **2018**, *47* (9), 3265–3300. https://doi.org/10.1039/C8CS00084K.

(42) Lin, Z.; Liu, Y.; Halim, U.; Ding, M.; Liu, Y.; Wang, Y.; Jia, C.; Chen, P.; Duan, X.; Wang, C.; Song, F.; Li, M.; Wan, C.; Huang, Y.; Duan, X. Solution-Processable 2D Semiconductors for High-Performance Large-Area Electronics. *Nature* **2018**, *562* (7726), 254–258. https://doi.org/10.1038/s41586-018-0574-4.

(43) Yuan, H.; Liu, X.; Ma, L.; Gong, P.; Yang, Z.; Wang, H.; Wang, J.; Yang, S. High

Efficiency Shear Exfoliation for Producing High-Quality, Few-Layered MoS2 Nanosheets in a Green Ethanol/Water System. *RSC Adv.* **2016**, *6* (86), 82763–82773. https://doi.org/10.1039/c6ra15310k.

(44) Liu, H.; Xu, L.; Liu, W.; Zhou, B.; Zhu, Y.; Zhu, L.; Jiang, X. Production of Mono- to Few-Layer MoS2 Nanosheets in Isopropanol by a Salt-Assisted Direct Liquid-Phase Exfoliation Method. *J. Colloid Interface Sci.* **2018**, *515*, 27–31. https://doi.org/10.1016/j.jcis.2018.01.023.

(45) Radha, S. K.; Crowley, K.; Holler, B. A.; Gao, X. P. A.; Lambrecht, W. R. L.; Volkova, H.; Berger, M.-H.; Pentzer, E.; Pachuta, K. G.; Sehirlioglu, A. Ultrathin 2D-Oxides: A Perspective on Fabrication, Structure, Defect, Transport, Electron, and Phonon Properties. *J. Appl. Phys.* **2021**, *129* (22), 220903. https://doi.org/10.1063/5.0051093.

(46) Dalle Feste, P.; Crisci, M.; Barbon, F.; Tajoli, F.; Salerno, M.; Drago, F.; Prato, M.; Gross, S.; Gatti, T.; Lamberti, F. Work Function Tuning in Hydrothermally Synthesized Vanadium-Doped MoO3 and Co3O4 Mesostructures for Energy Conversion Devices. *Appl. Sci.* **2021**, *11* (5), 2016. https://doi.org/10.3390/app11052016.

(47) Giannozzi, P.; Baroni, S.; Bonini, N.; Calandra, M.; Car, R.; Cavazzoni, C.; Ceresoli, D.; Chiarotti, G. L.; Cococcioni, M.; Dabo, I.; Corso, A. D.; Gironcoli, S. de; Fabris, S.; Fratesi, G.; Gebauer, R.; Gerstmann, U.; Gougoussis, C.; Kokalj, A.; Lazzeri, M.; Martin-Samos, L.; Marzari, N.; Mauri, F.; Mazzarello, R.; Paolini, S.; Pasquarello, A.; Paulatto, L.; Sbraccia, C.; Scandolo, S.; Sclauzero, G.; Seitsonen, A. P.; Smogunov, A.; Umari, P.; Wentzcovitch, R. M. QUANTUM ESPRESSO: A Modular and Open-Source Software Project for Quantum of Materials. *J. Phys. Condens. Matter* **2009**, *21* (39), 395502. https://doi.org/10.1088/0953-8984/21/39/395502.

(48) Hamann, D. R. Optimized Norm-Conserving Vanderbilt Pseudopotentials. *Phys. Rev. B* **2013**, *88*, 85117. https://doi.org/10.1103/PhysRevB.88.085117.

(49) Terentjev, A. V.; Constantin, L. A.; Pitarke, J. M. Dispersion-Corrected PBEsol Exchange-Correlation Functional. *Phys. Rev. B* **2018**, *98* (21), 214108. https://doi.org/10.1103/PhysRevB.98.214108.

(50) Bunău, O.; Joly, Y. Self-Consistent Aspects of x-Ray Absorption Calculations. *J. Phys. Condens. Matter* **2009**, *21* (34), 345501. https://doi.org/10.1088/0953-8984/21/34/345501.

(51) Guda, S. A.; Guda, A. A.; Soldatov, M. A.; Lomachenko, K. A.; Bugaev, A. L.; Lamberti, C.; Gawelda, W.; Bressler, C.; Smolentsev, G.; Soldatov, A. V.; Joly, Y. Optimized Finite Difference Method for the Full-Potential XANES Simulations: Application to Molecular Adsorption Geometries in MOFs and Metal–Ligand Intersystem Crossing Transients. *J. Chem. Theory Comput.* **2015**, *11* (9), 4512–4521. https://doi.org/10.1021/ACS.JCTC.5B00327.

(52) Hanlon, D.; Backes, C.; Higgins, T. M.; Hughes, M.; O'Neill, A.; King, P.; McEvoy, N.; Duesberg, G. S.; Mendoza Sanchez, B.; Pettersson, H.; Nicolosi, V.; Coleman, J. N. Production of Molybdenum Trioxide Nanosheets by Liquid Exfoliation and Their Application in High-Performance Supercapacitors. *Chem. Mater.* **2014**, *26* (4), 1751–1763. https://doi.org/10.1021/cm500271u.

(53) Dutta, S.; Pal, S.; De, S. Mixed Solvent Exfoliated Transition Metal Oxides Nanosheets Based Flexible Solid State Supercapacitor Devices Endowed with High Energy Density. *New J. Chem.* **2019**, *43* (31), 12385–12395. https://doi.org/10.1039/c9nj03233a.

(54) Smith, R. J.; King, P. J.; Lotya, M.; Wirtz, C.; Khan, U.; De, S.; O'Neill, A.; Duesberg, G. S.; Grunlan, J. C.; Moriarty, G.; Chen, J.; Wang, J.; Minett, A. I.; Nicolosi, V.; Coleman, J. N. Large-Scale Exfoliation of Inorganic Layered Compounds in Aqueous Surfactant Solutions. *Adv. Mater.* **2011**, *23* (34), 3944–3948. https://doi.org/10.1002/adma.201102584.

(55) Sricharan, M.; Gupta, B.; Moolayadukkam, S.; Ramakrishna Matte, H. S. S. Exfoliation in a Low Boiling Point Solvent and Electrochemical Applications of MoO 3. *Beilstein J. Nanotechnol* **2020**, *2020*, 662–670. https://doi.org/10.3762/bjnano.11.52.

(56) Cunningham, G.; Lotya, M.; Cucinotta, C. S.; Sanvito, S.; Bergin, S. D.; Menzel, R.; Shaffer, M. S. P.; Coleman, J. N. Solvent Exfoliation of Transition Metal Dichalcogenides: Dispersibility of Exfoliated Nanosheets Varies Only Weakly between Compounds. *ACS Nano* **2012**, *6* (4), 3468–3480. https://doi.org/10.1021/nn300503e.

(57) Hernandez, Y.; Lotya, M.; Rickard, D.; Bergin, S. D.; Coleman, J. N. Measurement of Multicomponent Solubility Parameters for Graphene Facilitates Solvent Discovery. *Langmuir* **2010**, *26* (5), 3208–3213. https://doi.org/10.1021/la903188a.

(58) Coleman, J. N.; Lotya, M.; O'Neill, A.; Bergin, S. D.; King, P. J.; Khan, U.; Young, K.; Gaucher, A.; De, S.; Smith, R. J.; Shvets, I. V.; Arora, S. K.; Stanton, G.; Kim, H. Y.; Lee, K.; Kim, G. T.; Duesberg, G. S.; Hallam, T.; Boland, J. J.; Wang, J. J.;

Donegan, J. F.; Grunlan, J. C.; Moriarty, G.; Shmeliov, A.; Nicholls, R. J.; Perkins, J. M.; Grieveson, E. M.; Theuwissen, K.; McComb, D. W.; Nellist, P. D.; Nicolosi, V. Two-Dimensional Nanosheets Produced by Liquid Exfoliation of Layered Materials. *Science* **2011**, *331* (6017), 568–571. https://doi.org/10.1126/science.1194975.

(59) Paolucci, V.; Emamjomeh, S. M.; Nardone, M.; Ottaviano, L.; Cantalini, C. Two-Step Exfoliation of WS2 for NO2, H2 and Humidity Sensing Applications. *Nanomaterials* **2019**, *9* (10). https://doi.org/10.3390/nano9101363.

(60) Charles Hansen. *HANSEN SOLUBILITY PARAMETERS A User's Handbook Second Edition*; 2007.

(61) Li, H.; Zhang, Q.; Yap, C. C. R.; Tay, B. K.; Edwin, T. H. T.; Olivier, A.; Baillargeat, D. From Bulk to Monolayer MoS2: Evolution of Raman Scattering. *Adv. Funct. Mater.* **2012**, *22* (7), 1385–1390. https://doi.org/10.1002/adfm.201102111.

(62) Liu, G.; Komatsu, N. Readily Available "Stock Solid" of MoS_2 and WS_2 Nanosheets through Solid-Phase Exfoliation for Highly Concentrated Dispersions in Water. *ChemNanoMat* **2016**, *2* (6), 500–503. https://doi.org/10.1002/cnma.201600116.

(63) Lu, C.; Ma, J.; Si, K.; Xu, X.; Quan, C.; He, C.; Xu, X. Band Alignment of WS2/MoS2 Photoanodes with Efficient Photoelectric Responses Based on Mixed Van Der Waals Heterostructures. *Phys. status solidi* **2019**, *216* (20), 1900544. https://doi.org/10.1002/PSSA.201900544.

(64) Artur Ciesielski; Paolo Samorì. Graphene via Sonication Assisted Liquid-Phase Exfoliation. *Chem. Soc. Rev.* **2013**, *43* (1), 381–398. https://doi.org/10.1039/C3CS60217F.

(65) Claramunt, S.; Varea, A.; López-Díaz, D.; Velázquez, M. M.; Cornet, A.; Cirera, A. The Importance of Interbands on the Interpretation of the Raman Spectrum of Graphene Oxide. *J. Phys. Chem. C* **2015**, *119* (18), 10123–10129. https://doi.org/10.1021/ACS.JPCC.5B01590.

(66) Ji, F.; Ren, X.; Zheng, X.; Liu, Y.; Pang, L.; Jiang, J.; Frank, S. (; Liu,). 2D-MoO 3 Nanosheets for Superior Gas Sensors †. **2016**, *8*, 8696. https://doi.org/10.1039/c6nr00880a.

(67) Kim, M.; Alfano, A.; Perotto, G.; Serri, M.; Dengo, N.; Mezzetti, A.; Gross, S.; Prato, M.; Salerno, M.; Rizzo, A.; Sorrentino, R.; Cescon, E.; Meneghesso, G.; Di Fonzo, F.; Petrozza, A.; Gatti, T.; Lamberti, F. Moisture Resistance in Perovskite Solar Cells

Attributed to a Water-Splitting Layer. *Commun. Mater. 2021 21* **2021**, *2* (1), 1–12. https://doi.org/10.1038/s43246-020-00104-z.

(68) Shu-Wen Zheng; Lei Wang; Hai-Yu Wang; Chen-Yu Xu; Yang Luo; Hong-Bo Sun. Observation of Quantum-Confined Exciton States in Monolayer WS 2 Quantum Dots by Ultrafast Spectroscopy. *Nanoscale* **2021**. https://doi.org/10.1039/D1NR04868F.

(69) XiaoHan Wang; YingChao Liu; JinLong Ren; KunPeng Dou; XingQiang Shi; RuiQin Zhang. A Revised Mechanism of Band Gap Evolution of TMDC Nanotubes and Its Application to Janus TMDC Nanotubes: Negative Electron and Hole Compressibility. *J. Mater. Chem. C* **2021**, *9* (28), 8920–8929. https://doi.org/10.1039/D1TC02385C.

(70) Liu, H.; Lee, C. J. J.; Jin, Y.; Yang, J.; Yang, C.; Chi, D. Huge Absorption Edge Blue Shifts of Layered α-MoO3 Crystals upon Thickness Reduction Approaching 2D Nanosheets. *J. Phys. Chem. C* **2018**, *122* (22), 12122–12130. https://doi.org/10.1021/acs.jpcc.8b03340.

(71) Katan, C.; Mercier, N.; Even, J. Quantum and Dielectric Confinement Effects in Lower-Dimensional Hybrid Perovskite Semiconductors. *Chem. Rev.* **2019**, *119* (5), 3140–3192. https://doi.org/10.1021/acs.chemrev.8b00417.

(72) Siokou, A.; Leftheriotis, G.; Papaefthimiou, S.; Yianoulis, P. Effect of the Tungsten and Molybdenum Oxidation States on the Thermal Coloration of Amorphous WO3 and MoO3 Films. *Surf. Sci.* **2001**, *482–485* (PART 1), 294–299. https://doi.org/10.1016/S0039-6028(01)00714-2.

(73) Morales-Luna, M.; Tomás, S. A.; Arvizu, M. A.; Pérez-González, M.; Campos-Gonzalez, E. The Evolution of the Mo5+ Oxidation State in the Thermochromic Effect of MoO3 Thin Films Deposited by Rf Magnetron Sputtering. *J. Alloys Compd.* **2017**, *722*, 938–945. https://doi.org/10.1016/j.jallcom.2017.06.149.

(74) Berardino, C. Di; Bélteky, P.; Schmitz, F.; Lamberti, F.; Menna, E.; Kukovecz, Á.; Gatti, T. Controlled Size Reduction of Liquid Exfoliated Graphene Micro-Sheets via Tip Sonication. *Cryst.* **2020**, *10* (11), 1049. https://doi.org/10.3390/CRYST10111049.

(75) Tyurnina, A. V.; Tzanakis, I.; Morton, J.; Mi, J.; Porfyrakis, K.; Maciejewska, B. M.; Grobert, N.; Eskin, D. G. Ultrasonic Exfoliation of Graphene in Water: A Key Parameter Study. *Carbon* **2020**, *168*, 737–747. https://doi.org/10.1016/J.CARBON.2020.06.029.

(76) Yang, L. C.; Gao, Q. S.; Tang, Y.; Wu, Y. P.; Holze, R. MoO2 Synthesized by Reduction of MoO3 with Ethanol Vapor as an Anode Material with Good Rate Capability for the Lithium Ion Battery. *J. Power Sources* **2008**, *179* (1), 357–360. https://doi.org/10.1016/J.JPOWSOUR.2007.12.099.

(77) Pal, A.; Shah, S.; Devi, S. Microwave-Assisted Synthesis of Silver Nanoparticles Using Ethanol as a Reducing Agent. *Mater. Chem. Phys.* **2009**, *114* (2–3), 530–532. https://doi.org/10.1016/J.MATCHEMPHYS.2008.11.056.

(78) Macis, S.; Rezvani, J.; Davoli, I.; Cibin, G.; Spataro, B.; Scifo, J.; Faillace, L.; Marcelli, A. Structural Evolution of MoO3 Thin Films Deposited on Copper Substrates upon Annealing: An X-Ray Absorption Spectroscopy Study. *Condens. Matter* **2019**, *4* (2), 41. https://doi.org/10.3390/CONDMAT4020041.

(79) Tougerti, A.; Berrier, E.; Mamede, A.-S.; La Fontaine, C.; Briois, V.; Joly, Y.; Payen, E.; Paul, J.-F.; Cristol, S. Synergy between XANES Spectroscopy and DFT to Elucidate the Amorphous Structure of Heterogeneous Catalysts: TiO2-Supported Molybdenum Oxide Catalysts. *Angew. Chemie Int. Ed.* **2013**, *52* (25), 6440–6444. https://doi.org/10.1002/ANIE.201300538.

(80) Rhodes, D.; Chae, S. H.; Ribeiro-Palau, R.; Hone, J. Disorder in van Der Waals Heterostructures of 2D Materials. *Nat. Mater.* **2019**, *18* (6), 541–549. https://doi.org/10.1038/s41563-019-0366-8.

(81) Scalise, E.; Houssa, M.; Pourtois, G.; Afanas'ev, V.; Stesmans, A. Strain-Induced Semiconductor to Metal Transition in the Two-Dimensional Honeycomb Structure of MoS2. *Nano Res.* **2011**, *5* (1), 43–48. https://doi.org/10.1007/S12274-011-0183-0.

(82) Yang, A.; Blancon, J.-C.; Jiang, W.; Zhang, H.; Wong, J.; Yan, E.; Lin, Y.-R.; Crochet, J.; Kanatzidis, M. G.; Jariwala, D.; Low, T.; Mohite, A. D.; Atwater, H. A. Giant Enhancement of Photoluminescence Emission in WS2-Two-Dimensional Perovskite Heterostructures. *Nano Lett.* **2019**, *19* (8), 4852–4860. https://doi.org/10.1021/ACS.NANOLETT.8B05105.

(83) Li, C.; Wang, T.; Wu, Y.; Ma, F.; Zhao, G.; Hao, X. Fabrication of Two-Dimensional Nanosheets via Water Freezing Expansion Exfoliation. *Nanotechnology* **2014**, *25* (49), 495302. https://doi.org/10.1088/0957-4484/25/49/495302.

TOC Graphic

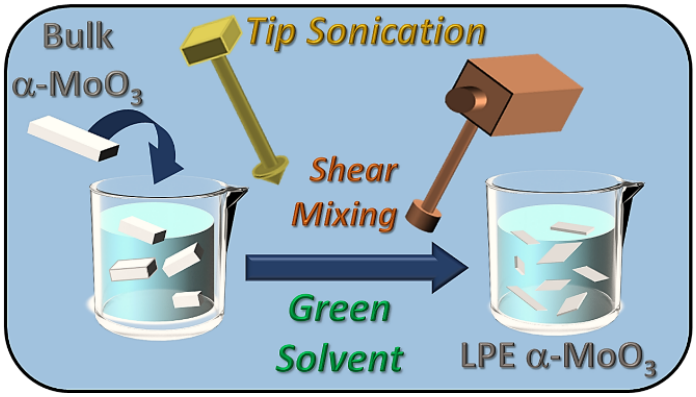
Bulk
α-MoO3
Tip Sonication
Shear
Mixing
Green
Solvent
LPE α-MoO3